Experiments in Fluids 27 (1999) 400–407 © Springer-Verlag 1999

Local convective heat transfer past the junction of channels of rectangular cross-section

F. Boizumault, S. Harmand, B. Desmet

Abstract An experimental study of the local convective heat transfer through the wall is presented in the case of an air flow past the junction of channels of a rectangular cross section. Tests for various flow-rate ratios through the two branches show that these ratios are not adequate to characterize the distribution of local heat transfer through the wall. The flow-rate through the side branch is a particularly significant parameter.

List of symbols

C	constant
D	hydraulic diameter (m)
e	resin thickness (m)
h	local convective heat transfer coefficient ($W\,m^{-2}\,K^{-1}$)
I	thermal radiation level
Nu	($=hD/\lambda$) local Nusselt number
NU	($=Nu/Nu_{fd}$) normalized Nusselt number
S	cross section area (m^2)
t	time (s)
T	temperature (°C or K)
V	mean velocity ($m\,s^{-1}$)
x, y, z	Cartesian coordinates (m)
x', y', z'	Cartesian coordinates (m)
X, Y, Z	($=x/D, y/D, z/D$) dimensionless coordinates

Greek symbols

ε	emissivity
λ	thermal conductivity ($W\,m^{-1}\,K^{-1}$)
ν	kinematic viscosity ($m^2\,s^{-1}$)
σ	Stefan–Boltzmann constant ($W\,m^{-2}\,K^{-4}$)
φ_{cd}	conductive heat flux ($W\,m^{-2}$)
φ_{cv}	convective heat flux ($W\,m^{-2}$)
φ_{rad}	radiative heat flux ($W\,m^{-2}$)
Ψ	flow-rate ratio

Received: *2 June 1998*/*Accepted*: *20 February 1999*

F. Boizumault, S. Harmand, B. Desmet
L.A.M.I.H. – Laboratoire de Mécanique et Energétique
E.N.S.I.M.E.V. – Université de Valenciennes et du Hainaut-Cambrésis
B.P. 311 – F-59304 Valenciennes Cédex
France

Correspondence to: B. Desmet

Subscripts

f	fluid
fd	fully developed
fl	air flow
p	resin plate
∞	outside the boundary layer

1 Introduction

Local convective heat transfer through the wall of channels of rectangular cross-section is studied in steady flow conditions past the junction of a rectilinear main channel with a side branch to which the flow is partially deviated (Fig. 1). The cross section is not very thick so the three dimensional effects are not very significant. Studies on junctions are mainly devoted to the determination of the corresponding head losses. This configuration may, for example, be encountered in turbo-alternators cooling channels.

Following the flow deviation towards the side branch, separation occurs in the side branch (1) with a recirculating zone area downstream from the rectangular corner. The recirculating zone area after the corner is larger than that in the case of a round corner junction (Idel'cik 1969). Close to the junction, the effective flow section is increased due to the fluid distribution among the two channels, and the result is a positive pressure gradient favorable to flow separation. The velocity reduction contributes to the generation of the recirculating zone (1) and can also be at the origin of flow separation in the rectilinear channel (2). The presence of a recirculating zone leads to free flow section reduction and then to flow divergence near reattachment.

In the side branch, the separation point corresponds to the corner edge. The shear flow region develops into a mixing zone between the recirculating flow and the free flow. Moreover, centrifugal forces corresponding to the flow deviation have a significant impact on the results. For a comparable geometry, Rieu et al. (1989), observed these effects, characterized by secondary flows.

Among the various separating and reattaching flow configurations, the backward facing step is well documented. In particular, Oki et al. (1993) directly solved the Navier–Stokes equation by numerical simulation. The results calculated with three different step ratios show that the recirculation zone becomes larger and the reattachment distance increases in proportion to the increase of the step ratio. Abe et al. (1994) used a modified version of the k–ε model to take the near-wall and low-Reynolds-number effects into account in both

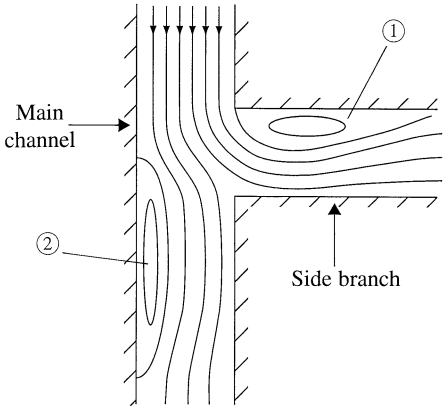

Fig. 1. Streamline distribution past a tee junction

attached and detached flows. The analysis of the effect of upstream boundary-layer thickness on the Stanton distribution shows that the peak value increases as the upstream boundary-layer thicknesses decrease. Heyerichs and Pollard (1996) studied both separating and impinging turbulent flows with heat transfer. They compared the performance of k–ε and k–ω turbulence models. The results indicate that the k–ω model demonstrates superior performance of prediction of convection heat transfer in complex turbulent flows.

The present study deals with convective heat transfer from the side channel wall within the aerodynamically perturbed zone.

2
Experimental description

2.1
Procedure for the determination of the local convective heat transfer

The knowledge of temperature or heat flux distributions on the surface of a solid body is sufficient, in a steady state, to solve the heat conduction equation in the considered field. In the present study a plate made of low conductive material has been used. This plate is heated on one side and subjected to the aerodynamically perturbed flow on the other side (Fig. 2.). The latter behaves as a thermally thick wall. The consequence of the non-uniform heat flux distribution is a non-uniform temperature distribution and the local heat flux through the wall to the air can be obtained from temperature distribution on the plate surface.

The heat conduction inside the plate is described by the standard Laplace equation:

$$\frac{\partial^2 T}{\partial x^2}+\frac{\partial^2 T}{\partial y^2}+\frac{\partial^2 T}{\partial z^2}=0 \tag{1}$$

The temperatures measured on the plate surface are used as boundary conditions (Fig. 2):

- For $z=0$, $T_0(x, y)$ is obtained by infrared thermography.
- For $z=-e$, $T_e(x, y)$ is deduced from temperature measurements with thermocouples.
- Other surfaces are considered adiabatic.

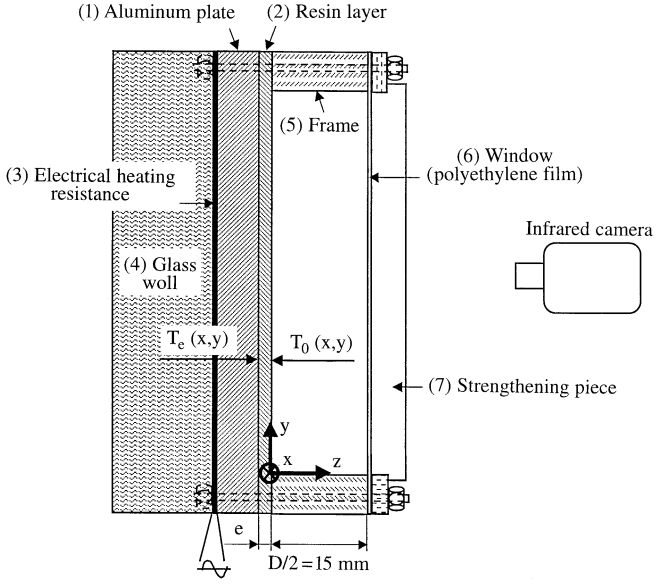

Fig. 2. Section of the lateral channel

Equation (1) is solved by using a finite element computer software and the heat flux through the wall is given by the following equation:

$$\varphi_{cd}=\lambda_p\left(\frac{\partial T}{\partial z}\right)_{z=0}=\varphi_{cv}+\varphi_{\mathrm{rad}} \tag{2}$$

where $\varphi_{cv}=h\ (T_0(x, y)-T_{fl})$ is the local convective heat flux and $\varphi_{\mathrm{rad}}=\varepsilon_p\sigma(T_0^4(x, y)-T_\infty^4)$ the radiative heat flux out of the plate to the environment. T_∞ denotes the test room temperature and T_{fl} the air temperature upstream of the junction and chosen as reference temperature. The comparison of the φ_{rad} values obtained by using the radiosity method and the equation given here, shows that the uncertainty in the φ_{rad} is less than 3% (Boizumault 1998). The local Nusselt number is deduced from eq. (2):

$$Nu=\left[\frac{\lambda_p(\partial T/\partial z)_{z=0}-\varepsilon_p\,\sigma(T_0^4(x,z)-T_\infty^4)}{T_0(x, y)-T_{fl}}\right]\frac{D}{\lambda_f} \tag{3}$$

where D is the hydraulic diameter of the side branch considered to be twice the channel width.

2.2
Experimental set up

The test rig is composed of two rectangular channels with the same width and assembled to constitute a tee junction (Fig. 3). Air enters the vertical channel and is then partially or totally deviated towards the side branch. Air flow is produced by fans installed with intermediate tanks at the end of each branch. The vertical channel upstream from the junction is 250 mm long and the horizontal channel is 1400 mm long. Sections of channels I and II are 15×180 and 15×150 mm^2 respectively. Intake III has an elliptic shape with a ratio between axes equal to 2. The design of test Sect. IV is given in Fig. 2. The test plate is composed of a thick aluminum plate (1) separated from the flow by a low thermal conductivity resin layer (2) heated by

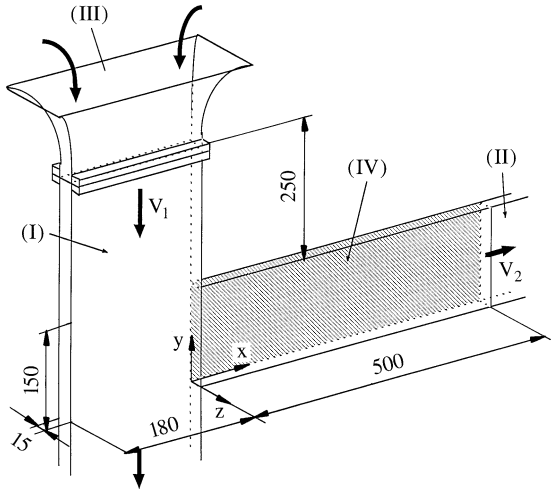

Fig. 3. Test configuration

electric resistance (3) on the other side with a glass wool protection (4) to reduce heat losses. A window (6, 7), separated from the test plate by a frame (5), mesures the temperature on the test plate surface by infrared thermography.

The test plate ($190 \times 500 \times 16$ mm^3) is one of the walls of the horizontal channel close to the junction. It is the grey zone in Fig. 5. The resin layer (2) is $e = 4$ mm thick. It is obtained by polymerization of the liquid resin directly on the aluminum plate with a final thermal conductivity $\lambda_p = 0.25$ W K^{-1} m^{-1}. The aluminum plate's function is to ensure uniform temperature distribution during the tests on the resin layer in contact with the aluminum plate. The window is made of a polyethylene film (6) glued onto the frame. Four strengthening pieces (7) spaced 100 mm from each other are used to limit the bending of the polyethylene film under the action of the outer pressure and it is not possible to measure temperature close to these pieces. The transmissivity of the polyethylene film has been found approximately equal to 0.85 (Boizumault et al. 1996).

2.3
Temperature measurement

Ten type *K* thermocouples are used to measure the temperature in the aluminum plate close to the resin layer. The temperature difference of the two faces of the resin layer varies between 5 and 30°C, depending on the test, whereas the maximum temperature difference between the thermocouples does not exceed ± 0.2°C. This shows that the aluminum plate ensures satisfactory temperature uniformity of the resin interface. The temperature of the resin surface in contact with the air flow is measured using infrared thermography (Fig. 2). A short wave, wide band (2–5 μm) camera equipped with a $20 \times 12.5^\circ$ lens was used with an image acquisition frequency of 20 Hz and a definition of 204×128 pixels. The camera's signal was subjected to oversampling. In the experimental conditions using the total lens aperture (20°), there are 28 temperature measurement points on the resin plate, which correspond to the spatial resolution of the camera. The thermal resolution is equal to 0.1% at 30°C but is lowered to ± 0.02% by the average of 32 images. For a black body at temperature T, observed through an ideally transparent medium, the thermal level signal $I(T)$ is delivered by the camera. Because of the partial transmission through the polyethylene film and the fluid absorption, the signal received by the camera is attenuated (Pajani 1989). Moreover, the surrounding reflection on the resin plate is a part of the given signal. To maximize the resin direct emission in comparison with the reflected disturbing flux, the resin layer is covered with a coat of black paint in order to increase the surface emissivity to $\varepsilon_p = 0.93$, estimated by calibration. Concurrence between the thermal level given by the camera and the actual resin plate surface temperature is obtained by calibration (Boizumault et al. 1996).

The air temperature variation between inlet and outlet remains less than 3°C for a difference T_0–T_{fl} equal to 40°C approximately in the less favorable situation. Using the temperature T_{fl} as a reference instead of the local fluid temperature over the resin does not introduce significant modification of the local Nusselt number value.

2.4
Velocity measurement

The flow-rates in the two branches are obtained by measuring velocity distributions in particular sections of the main branch and the lateral branch. Velocity distribution along the z'-axis orthogonal to the vertical channel wall in the section just downstream from the elliptic inlet nozzle (Fig. 3) is plotted in Fig. 4a and shows four different mean velocities V_1 in the first part of the vertical channel. The velocity distribution outside the boundary layer can be considered as uniform. Velocity distribution along the y'-axis, corresponding to the section length, is quite uniform too (Fig. 4b). The channel length upstream from the side branch is only 10 hydraulic diameters and this has a significant influence on the flow field upstream from the side branch. Figure 4 however, shows that the flow towards the side branch is not at the origin of an unsymmetrical velocity profile in the section just downstream of the inlet nozzle (Adams and Johnston 1988; Vogel and Eaton 1985). The mean velocity V_2, when the flow is totally deviated towards the horizontal channel, is obtained by averaging the velocity profiles measured by hot-wire anemometry in the section $x = 1220$ mm ($X = 40.7$) downstream from the junction. Figure 5 shows the non-uniformity of the velocity distribution in this section due to the presence of the flow separation generated by the junction.

Particle Imaging Velocimetry (PIV) is used to obtain the flow field in the side branch. Seeding particles are water droplets produced by the vibration of a piezoelectric ceramic in the ultrasonic frequency domain. The polyethylene window has been replaced by a Plexiglas plate. The air velocity in the pulsed laser sheet is obtained by determining particle displacement over time using a double-pulsed laser technique. The laser light sheet illuminates the flow in the plane equally spaced from the two large walls of the lateral branch and the positions of particles in that plane are recorded by the camera. The two laser pulses with a short time interval (100–150 μs) give two images of the particles. The velocity vector field in the plane is obtained by using a cross-correlation technique between both images. The final result in Fig. 6 is an average of six flow fields in the same conditions.

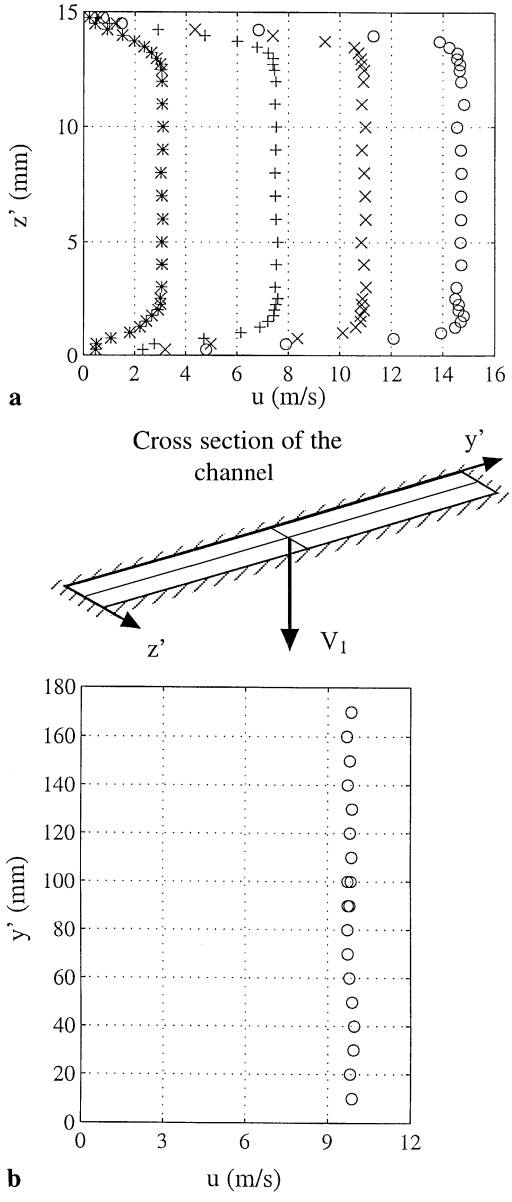

Fig. 4a,b. Main channel velocity distribution in the section downstream of the elliptic nozzle: **a** along the z'-axis, **b** along the y'-axis ($z' = 7.5$ mm)

3 Results

The estimation of uncertainty in the Nusselt number gives $\Delta h/h = \pm 8\%$ (Boizumault 1998). The experimental conditions are given in Table 1. The test classification, 1–13, is related to decreasing velocity V_2 ($3.5 < V_2 < 10$ m s^{-1}) and increasing velocity V_1 ($3.2 < V_1 < 14$ m s^{-1}). The corresponding Reynolds numbers $Re_1 = V_1 D/v_f$ ($6300 < Re_1 < 27500$) and $Re_2 = V_2 D/v_f$ ($7500 < Re_2 < 19000$), as well as the flow rate ratio $\Psi = (V_1 S_1)/(V_2 S_2)$ ($0.25 < \Psi < 1$), are also given in Table 1. The values of the Nusselt number Nu_{fd} in fully developed steady flow are in the last column of the table. These asymptotic values which correspond to the flow between two plates far from the channel inlet have been estimated with the aid of the Sparrow and Cur correlation (1982).

The convective heat transfer distribution on the plate is two-dimensional and its representation is not easy. Nusselt number isolines on the test plate surface are shown in Fig. 6 for six specific tests. For example, in case no. 12, two zones with very different Nusselt numbers can be observed. The low heat transfer zone where $Nu < 6$ spreads over approximately 30% of the test surface for $X < 5$. The order of magnitude of the heat transfer coefficient is $h = 0.9 \times Nu$. Time average velocity vectors obtained by P.I.V. are shown in the same figure where it can be observed that the flow deviates rapidly to the horizontal direction x. A significant velocity gradient in the y direction is a characteristic of the transition region between the recirculating flow and the free flow. Nusselt number isolines appear to be quite similar to the streamlines in the centre of the channel. Significant non-uniformity of the velocity profile (Fig. 5) is still present far from the junction at $X = 40.7$. The two-dimensional behaviour of the flow through the channel seems to be a consequence of the significant ratio between the height and width of the channel section equal to 10. This analogy between velocity and local Nusselt number is also observed for the other tests presented in Fig. 6.

Profiles of the normalized Nusselt number $NU = Nu/Nu_{fd}$ corresponding to test 12 are plotted in Fig. 7a. Vertical lines X_1–X_5 correspond to the sections equally spaced between the reinforcing pieces of the window. The same profiles are shifted between them in Fig. 7b. In the section studied, curves localize three zones: the recirculating zone where the heat transfer is low and rather constant, the mixing zone with a strong heat transfer gradient and finally the free flow where the heat transfer is greater. These profiles show the mixing zone development spreading downstream. Increasing distance between curves of constant velocity is a characteristic of the mixing zone development (Fig. 6). In the recirculating zone, the weak heat transfer slowly and regularly increases depending on the axial distance. However, taking for example test no. 12, in section X_5 where $Y > 3.3$, a significantly greater value of the Nusselt number is observed close to the upper wall. According to Fig. 6, this fact can be justified by the flow reattachment. Figure 8, corresponding to test no. 12, shows four reduced Nusselt number longitudinal profiles for $Y_1 = 1$, $Y_2 = 2$, $Y_3 = 3$ and $Y_4 = 4$. NU profile for Y_4 in the upper part of the channel increases more rapidly with the axial distance along the last segment ($13.3 < X < 16.7$).

The experimental situations are summarized in Fig. 9 using the following parameters: velocities V_1, V_2 and the ratio Ψ. There are four groups for V_2 and five groups for V_1. The results are illustrated by curves showing the normalized Nusselt number NU distribution on the side channel wall over the height of the channel. The results are presented in Fig. 10 with the same layout as in Fig. 9. Influence of V_1, V_2 and Ψ can be analyzed from Fig. 10. By using NU, the comparison between tests becomes independent from the velocity V_2.

It is generally considered that head loss is related to the size of the recirculating zone: the convergent effect and then the divergent effect due to the flow reattachment are considered to characterize the head loss. For a given geometry, the head loss, due to the junction, is often assumed to be a function depending only on the flow rate ratio (Idel'cik 1969). Therefore, the flow rate ratio is representative of the recirculating zone size.

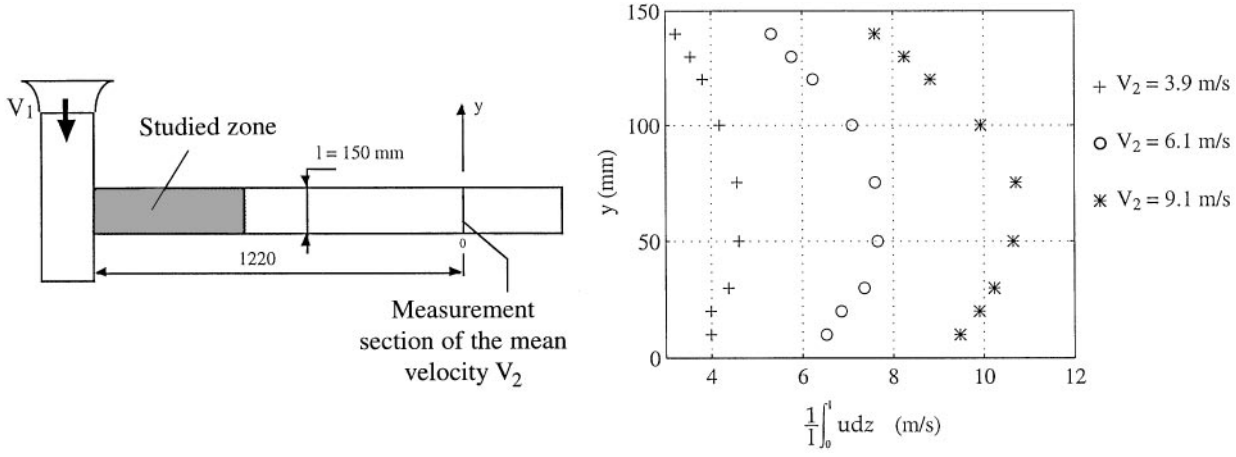

Fig. 5. Transverse mean velocity distribution downstream of the junction (side channel $x = 1220$ mm)

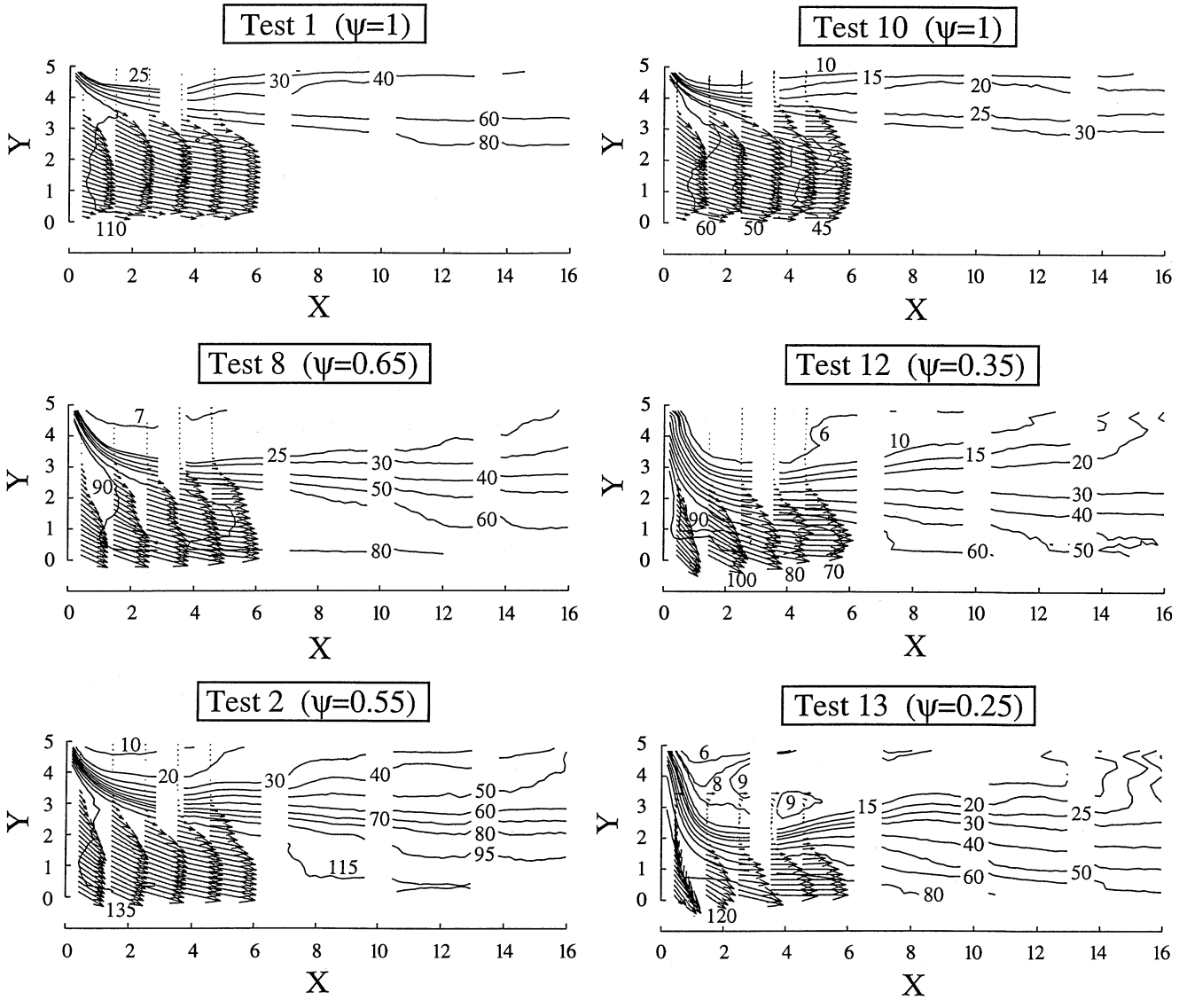

Fig. 6. Mean velocity obtained by P.I.V. and Nusselt number isolines

Table 1. Test conditions

Test no.	V_1 [m/s]	V_2 [m/s]	Re_1	Re_2	ψ	Nu_{fd}
1	8.2	9.8	15770	18850	1	50.1
2	14	9.5	27090	18380	0.55	48.8
3	6.5	7.8	12525	15030	1	41.9
4	8.2	7.8	16100	15310	0.8	42.5
5	14	7.4	27570	14570	0.45	41
6	4.2	5	8075	9610	1	29.8
7	5.5	5.7	10640	11030	0.85	33.3
8	8.2	6.6	16100	12955	0.65	37.4
9	14	5	27090	9675	0.3	30
10	3.25	3.9	6260	7500	1	25
11	5.5	3.9	10640	7625	0.6	25
12	8.2	3.6	16400	12600	0.35	23.3
13	14	4.3	27550	8460	0.25	26.5

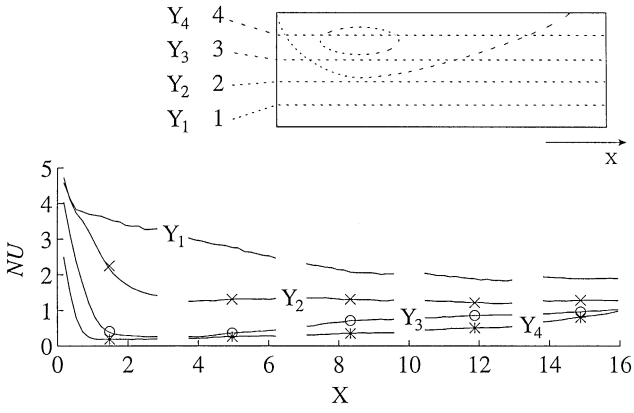

Fig. 8. Longitudinal normalized Nusselt number *NU* profiles (test 12)

– case $\Psi = 1$ (tests nos. 1, 3, 6, 10)

In the initial analysis, three zones can be defined from transverse Nusselt number distributions: the recirculating zone, the mixing region and the free flow. In the present situation the flow is totally deviated towards the side branch and the recirculating zone is small. With exception of the first segment ($X < 3.3$), the heat transfer remains rather intensive within the recirculating zone ($NU \neq 1$). In the free flow domain, *NU* is quasi uniform. The heat transfer in the mixing region varies (Fig. 10 X_1 profile) rapidly from the value in the recirculating zone to the constant value in the free flow. The normalized Nusselt number distributions over the height of the channel seem to converge to an asymptotic profile when V_2 is increased. This behavior should be related to the transition to turbulent flow.

– case $0.55 \leqslant \Psi < 1$ (tests nos. 2, 4, 7, 8, 11)

Excluding test no. 11, the general shape of the transverse profile of the Nusselt number remains similar when Ψ is varied from 0.55 to 1. The low heat transfer zone expands when Ψ is decreased and the mixing layer thickness seems to increase more rapidly downstream, spreading over the free flow and the recirculating zone.

– case $\Psi \leqslant 0.45$ (tests nos. 5, 9, 12, 13)

As the flow-rate ratio decreases, it becomes increasingly difficult to distinguish the mixing layer and the free flow by observing the normalized Nusselt number *NU* profile. The X_5 profile is different from the other profiles: the increase in the *NU* distribution in the upper part of the zone studied corresponds to an increase in the heat flux and is a consequence of the flow reattachment. In cases corresponding to $\Psi \leqslant 0.45$, the *NU* values near the upper wall given by the X_5 profile are higher than for the other profiles. As the flow-rate ratio becomes sufficiently small, a region with very low heat flux can be observed on the wall next to the corner where the flow is detached.

Normalized Nusselt number isolines are plotted in Fig. 11. for tests nos. 2,5,9,13, for which the velocity is fixed at $V_1 = 14$ m s^{-1}. It examines how the low heat exchange surface develops when $NU = 0.4$. To indicate the order of magnitude, $NU = 0.33$ (test no. 13, Fig. 11) which corresponds to a heat transfer coefficient $h \approx 8$ W m^{-2} K^{-1}. For test no. 13 with $\Psi = 0.25$, the low heat flux region spreads a lot over the plate studied and this development can be related to a lower efficiency of the momentum exchange inside the mixing region and a poor air replacement in the recirculating zone. The low

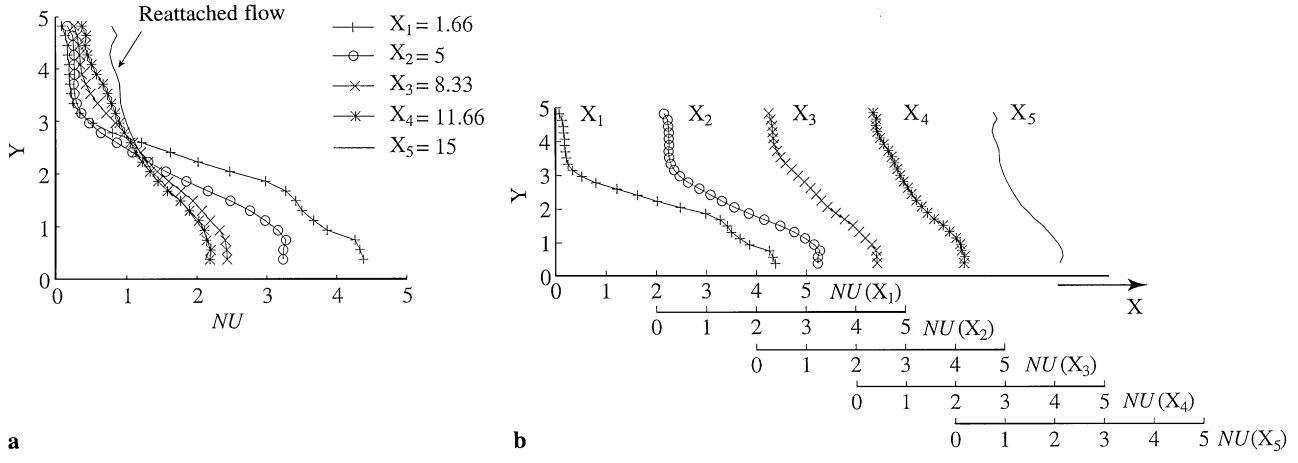

Fig. 7a,b. Transverse normalized Nusselt number *NU* distribution (test 12): **a** without translation, **b** after translation

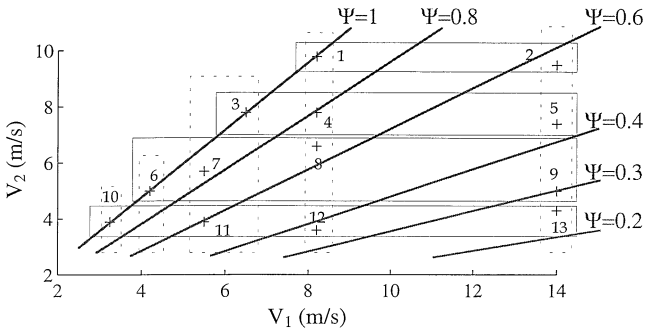

Fig. 9. Measurement conditions in the main channel and side channel

heat transfer surface associated to the recirculation zone decreases at a constant velocity V_1 and increasing V_2 (tests nos. 13,9,5,2) until $\Psi = 1$ is finally reached. Reciprocally, when velocity V_1 is increased while V_2 is maintained constant, the opposite behavior is observed because the flow-rate ratio is decreasing. For a given Ψ value, when V_2 is sufficiently significant, the *NU* profiles become very similar as V_2 increases. For tests nos. 11 and 12 (Fig. 10), the Nusselt number profiles are similar whereas the corresponding flow rate ratios are quite different (respectively 0.6 and 0.35). This similarity means that for the particular velocity, $V_2 = 4$ m s^{-1}, the increase in the velocity V_1 inside the rectilinear channel does not influence the shape of the low heat transfer region. Consequently, the flow-rate ratio Ψ is not the sole parameter that controls the normalized Nusselt number distribution, unlike the head loss coefficient. In the particular case $\Psi = 1$, velocity V_2 seems to control the normalized Nusselt number distribution. V_2 should characterize the different flow regimes and, consequently, the different heat transfer processes. This influence of V_2 can explain the fully different distributions observed for tests 11 and 2 whereas the flow-rate ratio remains nearly the same.

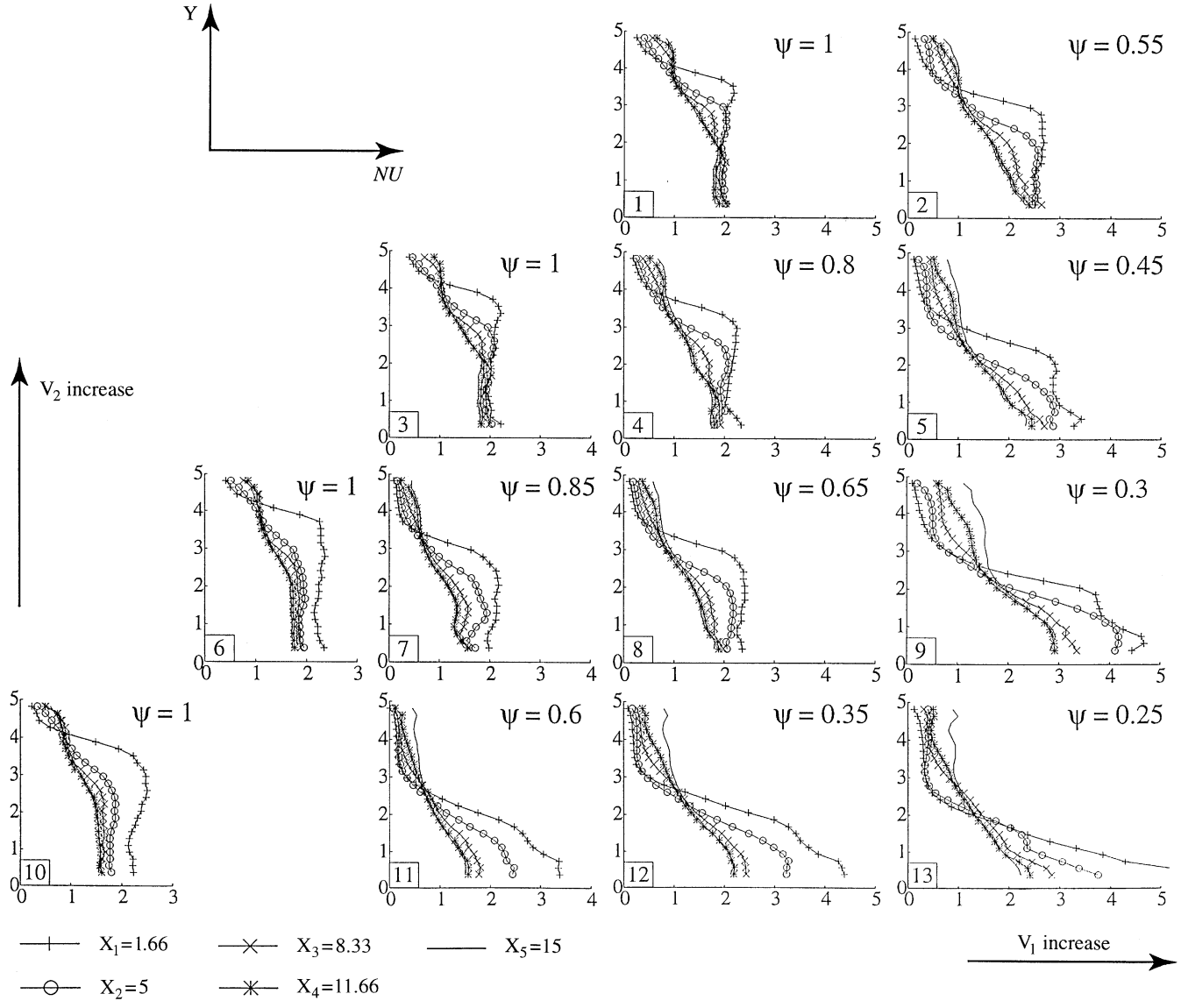

Fig. 10. Normalized Nusselt number *NU* distribution in the lateral branch downstream of the junction for various flow rate ratios

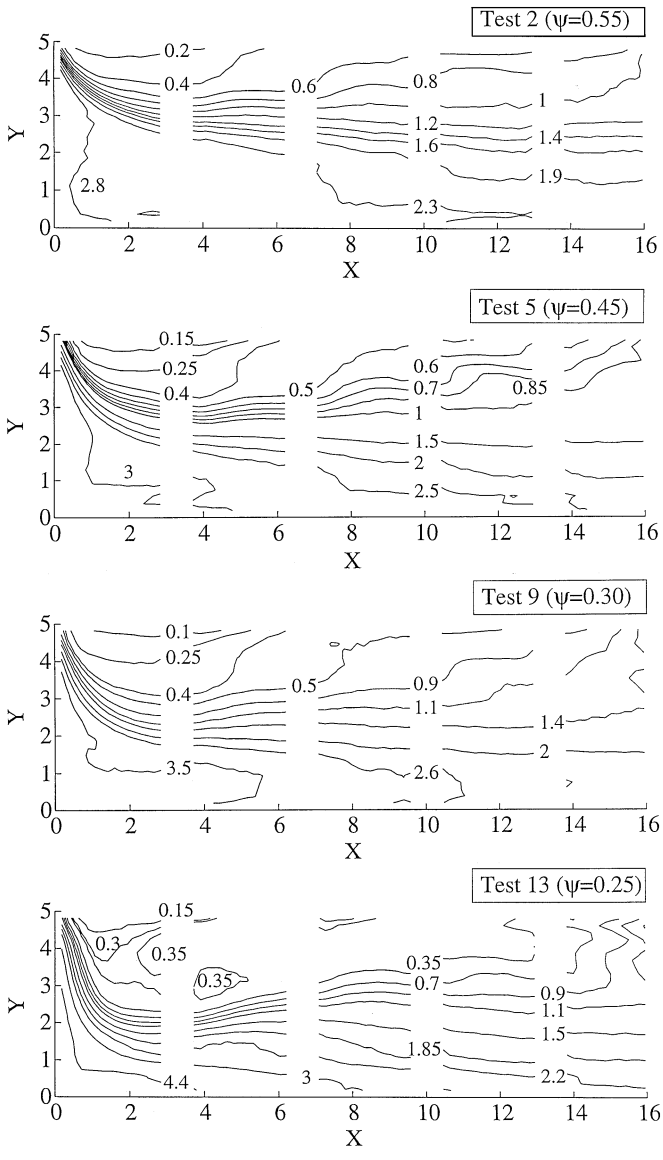

Fig. 11. Development of the low convective heat transfer region

4
Conclusion

The experimental method developed in the present work has been used to determine the local convective heat transfer through the wall in the specific case of the partially or totally deviated flow towards the side branch of a tee junction in steady conditions. The comparison of the Nusselt number distribution with the time averaged flow pattern midstream, obtained by Particle Image Velocimetry, reveals the similarity between the two distributions. Three distinct convective regions exist: the recirculating zone, mixing zone and free zone. This study shows that the heat flux through the wall to the recirculating flow remains low and is higher in the free flow. In the case of the geometry studied, the different flow regions seem to be linked with the convective heat transfer distribution. The *NU* distribution can be classified into 5 classes in terms of V_1 and 4 in terms of V_2, each with Ψ as the parameter.

Moreover, the analysis of flow conditions corresponding to different flow-rate ratio shows that this parameter is not sufficient to characterize the local convective heat transfer. In particular, the test results clearly show the influence of the mean velocity of the flow through the side branch on the convective heat transfer distribution.

References

Abe K; Kondoh T; Nagano Y (1994) A new turbulence model for predicting fluid flow and heat transfer in separating and reattaching flows. Int J Heat Mass Transfer 37: 139–151

Adams EW; Johnston JP (1988) Effects of the separating shear layer on the reattachment flow structure. Exp Fluids 6: 493–499

Boizumault F (1998) Contribution à l'étude expérimentale du transfert de chaleur local par convection forcée dans le cas d'écoulements présentant une zone de recirculation. Thèse de doctorat de l'Université de Valenciennes et du Hainaut-Cambrésis, no. 98-12

Boizumault F; Harmand S; Desmet B (1996) Experimental determination of the local heat transfer coefficient on a thermally thick wall downstream a backward-facing step. Proceedings of Eurotherm Seminar QIRT 50: 141–146

Heyerichs K; Pollard A (1996) Heat transfer in separated and impinging turbulent flows. Int J Heat Mass Transfer 39-12: 2385–2400

Idel'cik IE (1969) Memento des pertes de charges. In: Collection de la direction des études et recherches d'Electricité de France. (ed Eyrolles), Paris

Oki M; Iwasawa T; Suehiro M; Umeda T; Nakayama Y; Aoki K (1993) Numerical simulation without turbulence model for backward facing step flow. JSME Int J/B 36-4: 577–583

Pajani D (1989) Mesure par thermographie infrarouge. (ed ADD) Le plessis Robinson, France

Rieu R; Pelissier R; Farahifar D (1989) An experimental investigation of flow characteristics in bifurcation models. European J Mech B/Fluids 8: 73–101

Sparrow N; Cur N (1982) Turbulent heat transfer in a symmetrically or asymmetrically heated flat rectangular duct with flow separation at inlet. J Heat Transfer 104: 82–89

Vogel IC; Eaton JK (1985) Combined heat transfer and fluid dynamic measurement dowstream of a backward-facing step. J Heat Transfer 6: 922–929